Time-resolved interferometric detection of ultrashort strain solitons in sapphire

P. J. S. van Capel and J. I. Dijkhuis*
Section Nanophotonics, Debye Institute for Nanomaterials Science, University of Utrecht, P.O. Box 80000, 3508 TA Utrecht, The Netherlands

(Received 12 November 2009; revised manuscript received 23 March 2010; published 13 April 2010)

We study one-dimensional nonlinear propagation of high-amplitude acoustic waves in sapphire, for various sample temperatures, sample thicknesses, and pump fluences. Strain waves are generated in a 100-nm-thick chromium film and launched into the sapphire. For temperatures <60 K, damping can be neglected and propagation is dominated by the nonlinear and dispersive properties of the sapphire substrate. An interferometric technique is used to detect the wave on an epitaxially grown ~20-nm-thick Cr film at the opposite side of the sample. At the lowest temperature of 18 K, a train of up to seven solitons is detected in sapphire for a pump fluence of 11 $\mathrm{mJ/cm^2}$. From the soliton amplitudes and velocities, we infer soliton temporal and spatial widths as short as 200 fs and 2 nm. A theoretical analysis based on numerical solution of the Korteweg-de Vries-Burgers equation yields excellent agreement to all experiments presented. Deviations to the direct theoretical result can be explained by pump intensity variations, affecting the (nonlinear) propagation properties.

DOI: 10.1103/PhysRevB.81.144106 PACS number(s): 63.20.−e, 62.30.+d

I. INTRODUCTION

It is well known from elementary solid-state physics that high-frequency phonons in crystalline structures suffer from dispersion.[1] This dispersion was experimentally investigated for several solids and propagation directions.[2] When the strain amplitudes become sufficiently large, the harmonic approximation of the atomic potential is not valid anymore and higher-order elastic effects come into play.[3] This results in deformation of the strain wave and generation of higher frequencies. When damping can be ignored, it is the joint effect of nonlinearity and dispersion that leads to the formation of so-called acoustic *solitons*.

Solitons have been observed in numerous fields of physics.[4–7] A first theoretical description of the soliton was given by Korteweg and De Vries as early as 1895.[8] First experimental proof of acoustic solitons in solids was obtained by Hao and Maris[9] in 2001, using picosecond ultrasonics techniques. This groundbreaking work was followed by a series of picosecond ultrasonics experiments improving the understanding of acoustic wave propagation in the nonlinear and dispersive regime.[10–13] Muskens and Dijkhuis have used frequency-domain techniques to examine soliton propagation in sapphire and ruby,[14,15] and demonstrated soliton trains with frequency content exceeding 870 GHz.

In picosecond ultrasonics experiments, high-repetition-rate femtosecond lasers with inherent low available pump power (10 nJ per pulse) are used. Thus, narrow (<10 μm) pump beam waists are required to induce nonlinear effects. In that case, propagation can not be considered one dimensional anymore and nonlinear diffraction takes place.[16] The resulting transverse energy diffusion leads to decreased soliton generation efficiency and effectively two-dimensional propagation.[11,17]

Here, we present a series of time-resolved interferometric experiments on soliton generation using a high-power (1 mJ per pulse), 1 kHz repetition-rate laser system. The goal of the present experiments is to combine maximum nonlinear propagation effects with large diameter acoustic beams.[18] This way, the number of solitons is maximized while diffraction effects are reduced.

After discussing the setup and sample preparation details, interferometric amplitude and phase measurements are presented on three sapphire samples of various thicknesses. Propagation is monitored for a range of temperatures and pump intensities. The experimental traces are analyzed and discussed using both numerical modeling of nonlinear and dispersive effects, and exact theoretical results.

II. SAMPLE AND SETUP

A. Setup

The experimental geometry and sample design are sketched in the inset of Fig. 1(b). A 400 nm pump with a beam waist ($1/e^2$ intensity radius) of 170 μm ±5% hits a thin chromium film deposited on a sample slab to generate a thermoelastic strain pulse. The generated strain pulse shape is determined by temperature dynamics and the optical-absorption depth of the pump $\zeta_{pump}=11.2$ nm. A detailed discussion of these dynamics can be found elsewhere.[19] The initially generated pulse shape strongly deviates from the Gaussian derivative pulse Eq. (8) we assume in our numerical modeling. However, due to acoustic attenuation during propagation through the 100-nm-thick generation film, the pulse shape is smoothed to resemble a Gaussian derivative. This shape appears to form a faithful description for the used pump fluences. Additional nonlinear effects in the generation process are discussed in Sec. V A.

An 800 nm probe is focused to around 5 μm beam waist on a second thin chromium film at the opposite side of the sample to detect these strain pulses after propagation through the sample. The probe is configured to form a highly sensitive Sagnac interferometer,[20] allowing for measurement of both the time-dependent variation in relative reflectivity amplitude $\rho(t)$ and phase $\delta\varphi(t)$ induced by the strain $s(z',t)$ arriving in the metal film.

Reflectivity variations $\rho=\rho_{metal}$ and $\delta\varphi_{metal}$ originate from strain-induced changes in optical constants of the metal,

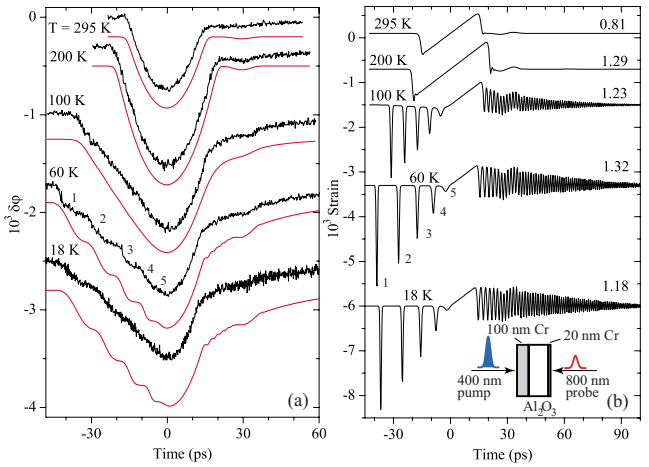

FIG. 1. (Color online) (a) Measured (black line) and calculated (red or gray line) phase signals for room temperature (upper trace), and cooling via 200, 100, 60 to 18 K (bottom trace) for a sapphire sample thickness of 307 μm and a constant pump fluence of 9.7 mJ/cm^2. Calculations include broadening effects. Numbers $i=1,\ldots,5$ at 60 K trace correspond to arrival of ith soliton at the detection surface. (b) Calculated strain wave shape after propagation through 307 μm of sapphire, given the input strain amplitude $s_0(\times 10^3)$ required to reach agreement with the measurements in (a). Inset: sketch of experimental geometry.

$$\rho_{metal}(t) = \int_0^{d_{probe}} f_\rho(z')s(z',t)dz', \tag{1}$$

$$\delta\varphi_{metal}(t) = \int_0^{d_{probe}} f_{\delta\varphi}(z')s(z',t)dz'. \tag{2}$$

Here, z' is the inward direction of the film, $z'=0$ at the film surface, d_{probe} the probe film thickness, and $f_\rho(z')$ and $f_{\delta\varphi}(z')$ represent the respective amplitude and phase sensitivity functions for Cr. The sensitivity functions are oscillatory and decay as $\exp(-z/\zeta_{probe})$, with $\zeta_{probe}=18.4$ nm the optical penetration depth at the probe wavelength of 800 nm. In our calculations, we have used $f_\rho(z')$ and $f_{\delta\varphi}(z')$ as determined by Saito *et al.*[21] for 830 nm, under the assumption of slowly varying optical properties for chromium in this wavelength range. Since the probe penetration depth is on the order of the probe film thickness d_{probe} of 20 nm, integration in Eqs. (1) and (2) occurs over a finite interval. Since the optical reflection coefficient at the Cr/sapphire interface is small, only 8%, and the probe intensity has already diminished by 65% at a depth of 20 nm, the additional effects observed by a probe reflection returning from the Cr/sapphire (and higher-order contributions returning from the sample) are only several percents of the primary contribution Eqs. (1) and (2), and are further neglected.

Additionally, the phase signal contains a contribution $\delta\varphi_{surface}(t)$, generally larger than $\delta\varphi_{metal}(t)$,[18] proportional to the surface displacement $\delta z'(t)$,

$$\delta\varphi_{surface}(t) = 2 \times \frac{2\pi}{\lambda}\delta z'(t). \tag{3}$$

The optical response in the phase signal for $\delta\varphi_{surface}(t)$ both with and without $\delta\varphi_{metal}(t)$ for a typical soliton signal is shown in Fig. 5(c). Qualitatively, the unipolar surface contribution due to a unipolar soliton distinguishes itself from the bipolar metal film contribution. The latter is more sensitive to arrival time variation, which proves to be an important effect in our experiments. The calculation result demonstrates that the surface contribution dominates the phase signal at the used probe wavelength. We have therefore chosen to analyze the measured phase signals as $\delta\varphi(t)=\delta\varphi_{surface}(t)$.

The low repetition rate of our laser system allows for normalization by a background measurement and ensures that we obtain absolute values for both ρ and $\delta\varphi$. For an integration time of 1 s, the typical noise level is 10^{-5} for both amplitude and phase signal (corresponding to surface displacements, present in the phase signal, on the order of 1 pm).

The sample is located in a continuous flow cryostat allowing the sample temperature to be set from 295 K (room temperature) to 5 K, with a stability of ± 0.1 K during a typical experimental run on a single sample. Experiments were performed at 295, 200, 100, 60, and 18 K. The interferometer was aligned such to prevent probe beam reflections off the cryostat windows to enter the detection system and reduce contrast. Pump fluences I_0 ranged from 1 to 12 mJ/cm^2 in steps of ~ 1 mJ/cm^2. Above 12 mJ/cm^2, measurements became unstable preventing measurement of clear soliton signals. Reasons for the instability will be discussed in Sec. V.

B. Samples and preparation

We have used three sapphire (Al_2O_3) (0001)-oriented samples (acoustic propagation along the sapphire c axis), with measured thicknesses d_{sample} of 123, 307, and 405 μm. Front and rear planes of the samples have angles of 0.089°, 0.064°, and 0.038°, respectively. Assuming a probe beam diameter of $2w_{probe}\sim 10$ μm, this results in a spread in arrival time τ_p of the strain pulses over the probe spot amounting to 1.39, 0.99, and 0.59 ps.

Since sapphire is transparent for the probe wavelength of 800 nm, a thin opaque film is required on the probe side to detect the presence of strain at the surface. Chromium films that were deposited in-house by thermal evaporation appeared to suffer from grain formation and interface scattering, resulting in strong phonon attenuation at frequencies >250 GHz.[11,22] Since the frequencies in a typical soliton wave packet may exceed 1 THz (Sec. IV), a good sample surface quality is essential to avoid high-frequency phonon scattering and attenuation.

For this reason, high-quality thin chromium films were grown for us by Dr. M. Highland in the group of Prof. Dr. D. Cahill at the University of Illinois at Urbana-Champaign. Films are grown epitaxially and are nearly single crystalline.[23] Attenuation is not limited by metal film grains or Cr/sapphire interface scattering but governed by intrinsic damping processes.[24,25] The thickness of the Cr probe films is $d_{probe}\sim 20$ nm while the Cr transducers at the pump side are $d_{pump}\sim 100$ nm thick.

Given film thickness and quality, we estimate the cutoff frequency for transmission through the probe metal film to be $(1/\tau_m)\gg 600$ GHz. The low impedance mismatch be-

tween Cr and sapphire leads to an estimated acoustic interface reflection coefficient of only 4%. Since the reflection coefficient is so low, multiple acoustic reflections in the pump and probe film are small compared to the primary response.

III. THEORY

A. Korteweg-de Vries-Burgers equation

In order to describe propagation of wave packets of high amplitude and containing high frequencies, one needs to include nonlinearity, lattice dispersion, and scattering with thermal phonons in the one-dimensional linear wave equation for propagation of a strain $s(z,t)$,

$$\frac{\partial^2 s}{\partial t^2} = v_s^2 \frac{\partial^2 s}{\partial z^2} - \frac{\alpha}{\rho}\frac{\partial}{\partial z}\left(s\frac{\partial s}{\partial z}\right) + 2v_s\beta\frac{\partial^4 s}{\partial z^4} + \frac{\eta v_s}{\rho}\frac{\partial^3 s}{\partial z^3}. \quad (4)$$

Here, ρ and v_s are the mass density and sound velocity in sapphire, respectively. The strength of the nonlinear term is measured by the nonlinearity constant $\alpha=-18.5\times10^{11}$ N/m^2 and that of the dispersion by the first-order dispersion parameter β, measured to be $(3.5\pm0.3)\times10^{-17}$ m^3/s along the sapphire c axis.[22] Scattering is characterized by the temperature-dependent viscosity parameter η (6×10^{-4} N s/m^2 at room temperature).

Transforming to the moving coordinate frame ($x=z-v_st$), one finds the Korteweg-de Vries-Burgers equation

$$\frac{\partial s}{\partial t} = -\frac{\alpha}{2\rho v_s}s\frac{\partial s}{\partial x} - \beta\frac{\partial^3 s}{\partial x^3} + \frac{\eta}{2\rho}\frac{\partial^2 s}{\partial x^2}. \quad (5)$$

Equation (5) can be solved numerically for an arbitrary input strain. In Sec. V, we discuss the initial conditions and the calculation details. For clarity, calculated strain profiles are presented together with the measured traces in Figs. 1–5.

Assuming one-dimensional propagation is an approximation since transverse intensity gradients lead to diffraction. In the two-dimensional case (cylindrical coordinate system), a diffraction term has to be added to Eq. (5), leading to the Kadomtsev-Petviashvili equation. However, for the current pump beam waist of 170 μm, sample thicknesses, and fluences we can safely neglect diffraction.[16]

B. Temperature dependence of damping term

When performing experiments at elevated temperatures, acoustic attenuation in the sapphire substrate plays an important role. Damping in sapphire shows a strong temperature dependence. Auld[25] reports a value of $\eta=6\times10^{-4}$ N s/m^2 at room temperature decreasing linearly with temperature and a frequency dependence $\propto\omega^{1.9}$. Pomerantz[26] and Ciccarello[27] have measured the acoustic attenuation in sapphire in the 0.5–10 GHz range below 130 K and a temperature dependence roughly $\propto T^4$ with a frequency dependence $\propto\omega$. The different behavior at these two temperatures is due to a transition from Akhieser damping to anharmonic phonon decay.[28,29] Below 10% of the Debye temperature Θ_D (980 K for sapphire), anharmonic phonon decay dominates. For a sample temperature of 200 K, we assume that Akhieser damping is still dominant and extrapolate the room-temperature value of η to 4×10^{-4} N s/m^2.

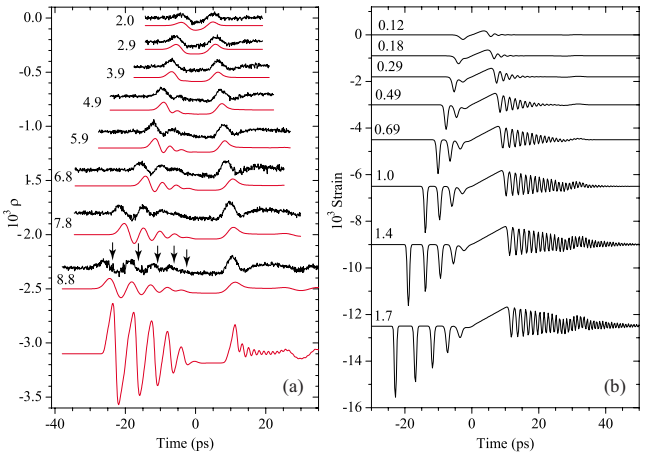

FIG. 2. (Color online) (a) Measurements (black line) and calculations (red or gray line) of amplitude (ρ) signal for wave propagation through 123 μm of sapphire at a temperature of 18 K. Numbers indicate pump fluence in mJ/cm^2. Bipolar features correspond to arrival of solitons. For 8.8 mJ/cm^2, soliton arrival times are indicated by arrows. In the calculation, corrections for temporal broadening discussed in Sec. V were included. At fluence of 8.8 mJ/cm^2, both uncorrected and corrected signals are shown, demonstrating the relevance of temporal broadening effects. (b) Calculated strain profiles after propagation for an input pulse of width ~3.6 ps and indicated strain amplitudes s_0 ($\times10^3$). At the highest fluence, at least five solitons are formed. Note that the final solitons in the calculation are not resolved in the measurement.

In the calculation for low temperatures, dependence $\propto\omega$ can be taken into account by replacing the damping term in Eq. (5) by $+2\alpha_0 v_s^2 \partial s/\partial x$.[30] From Pomerantz,[26] we have inferred a value for $\alpha_0 v_s^2$ of 1.0×10^{-1} m at 100 K. This value

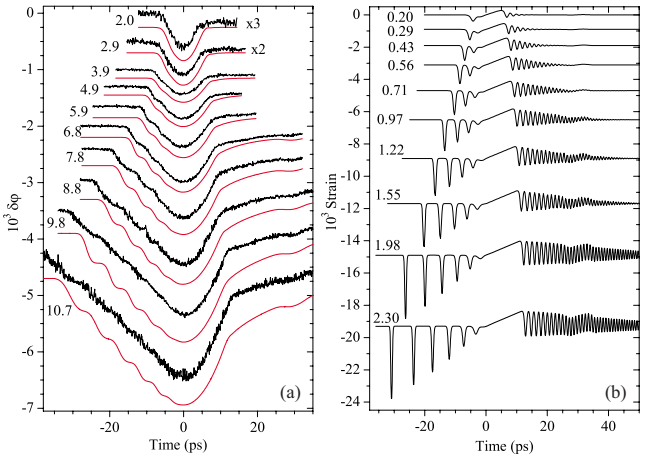

FIG. 3. (Color online) (a) Measured (black line) and calculated (red or gray line) phase ($\delta\varphi$) signals for the 123-μm-thick sample at 18 K. Numbers indicate fluence in millijoule per square centimeter. Steps correspond to soliton arrival at the detection surface. In the calculation, broadening effects discussed in Sec. V are taken into account. (b) Calculated strain wave form after propagation through 123 μm of sapphire. Numbers indicate input strain amplitude $s_0\times10^3$.

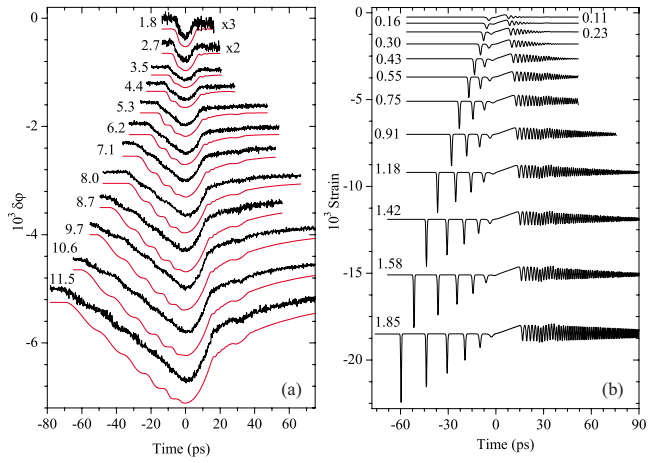

FIG. 4. (Color online) (a) Measured (black line) and calculated (red or gray line) $\delta\varphi$ signals for the 307-μm-thick sample at 18 K. Numbers indicate fluence in millijoule per square centimeter. In the calculation, broadening effects discussed in Sec. V are taken into account. (b) Calculated strain wave form after propagation through 307 μm of sapphire. Numbers indicate input strain amplitude $s_0 \times 10^3$.

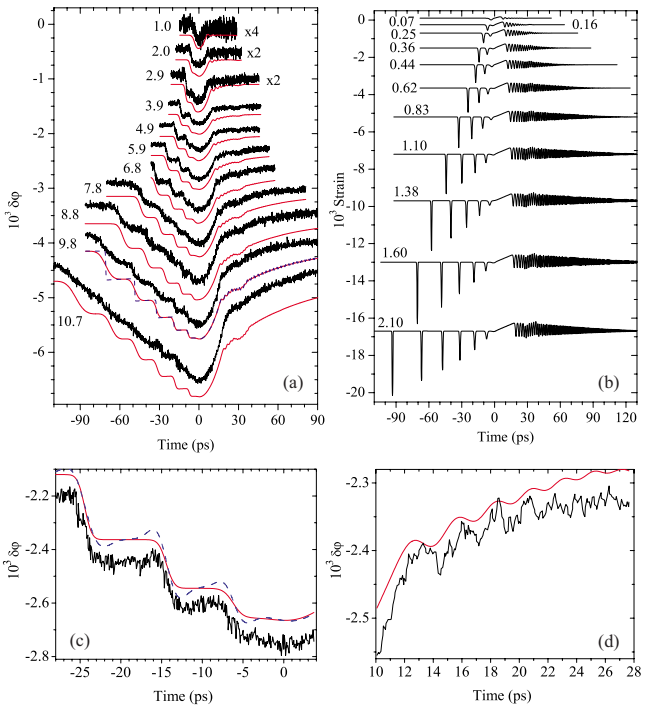

FIG. 5. (Color online) (a) Measured (black line) and calculated (red or gray line) $\delta\varphi$ signals for the 405-μm-thick sample at 18 K. Numbers indicate fluence in millijoule per square centimeter. In the calculation, broadening effects discussed in Sec. V are taken into account. Calculated data for fluence of 9.8 mJ/cm^2 shows difference between broadened (solid line) and unbroadened (dashed line) signals. (b) Calculated strain wave form after propagation through 405 μm of sapphire. Numbers indicate input $s_0 \times 10^3$. (c) Detail of solitons in measured trace at 5.9 mJ/cm^2, and calculation with and without metal film contribution (red solid and blue dashed line, respectively). The width w_1 of the first soliton was measured at ~500 fs. (d) ~500 GHz oscillations in the trailing part of the wave for 5.9 mJ/cm^2 and corresponding calculated result (red line).

was extrapolated to obtain faithful values at 60 and 18 K of our experiments.

For $T<100$ K, typical frequencies f_{tr} surviving traversal of a length d_{sample} in sapphire can be estimated as $f_{tr} \sim (2\pi\alpha_0 d_{sample})^{-1}$. For $d_{sample} \sim 300$ μm we find $f_{tr} = 1.3$ THz at 100 K and >10 THz at 60 K, indicating vanishing attenuation below 60 K. At 77 K, $f_{tr}=6.5$ THz, implying that soliton development and propagation are feasible at LN_2 temperatures in sapphire.

C. Compressive solitons

In the absence of damping, Eq. (5) reduces to the well-known Korteweg-de Vries (KdV) equation. Following the analysis of Muskens,[31] we rewrite the KdV equation into the more general form

$$\frac{\partial\psi}{\partial t'} = 6\sigma_N^2\psi\frac{\partial\psi}{\partial\xi} + \frac{\partial^3\psi}{\partial\xi^3} \tag{6}$$

with

$$\sigma_N \simeq \frac{\tau}{\sqrt{8}}\left(\frac{\alpha s_0 v_s}{12\rho\beta}\right)^{1/2}, \tag{7}$$

the similarity parameter for a Gaussian derivative input strain wave form

$$s(t) = s_0\frac{2\sqrt{e}}{\tau}t\exp\left(\frac{-2t^2}{\tau^2}\right). \tag{8}$$

A normalization of the compressive strain was performed.[31,32] For the compressive part of the input strain wave packet ($s<0$), exact solutions to Eq. (6) can be found:[9,10,31] a family of N so-called *solitons* with index number $i=1,\ldots,N$. For $\sigma_N \gg 1$, $\sigma_N \sim N$. The ith soliton is characterized by a single parameter (eigenvalue) λ_i, linking its velocity, amplitude, and width. In real-space coordinates, the soliton solutions have the form

$$s_i(x,t) = a_i\ \mathrm{sech}\ 2\left[\frac{(x-x_{0,i})-v_i t}{w_i}\right]. \tag{9}$$

$x_{0,i}$ is the projected soliton position at $t=0$ (virtual since the solitons are not yet formed at that time). The supersonic velocity v_i, an easily accessible experimental quantity, can be expressed in λ_i as

$$v_i = \frac{8\beta}{v_s^2\tau^2}\lambda_i \tag{10}$$

while the amplitude a_i and temporal width w_i in turn connect to v_i as

$$a_i = \frac{6\rho v_s}{\alpha}v_i(\alpha<0), \tag{11}$$

$$w_i = \frac{1}{v_s}\left(\frac{4\beta}{v_i}\right)^{1/2}. \quad (12)$$

For an initially sech^2-shaped compressive part of the strain, the eigenvalues λ_i can be calculated exactly:[32]

$$\lambda_i = (1 - 2i + \sqrt{1 + 4\sigma_N^2})^2. \quad (13)$$

For the tensile part of the strain (with $s > 0$), Eq. (6) is not integrable and does not give rise to discrete solutions of Eq. (6) but to a continuum of states. The development of the rarefaction part of the wave must therefore be evaluated numerically.

IV. EXPERIMENTAL RESULTS

For all presented measurements, the $t=0$ point was determined for each sample for low fluences as the point where either the $\delta\varphi$ or ρ signal was maximal, and chosen fixed for higher fluences. The calculated strain traces according to a numerical solution of Eq. (5), and taking into account the correct damping, are presented in Figs. 1(b), 2(b), 3(b), 4(b), and 5(b). The corresponding calculated ρ and $\delta\varphi$ traces are shown together with the measurements in Figs. 1(a), 2(a), 3(a), 4(a), and 5(a). Acoustic reflections at the pump film/substrate and substrate/probe film interface were taken into account. Measured traces were corrected for the reduced interferometer contrast of ~88% for the 123 and 307 μm samples, and ~50% for the 405 μm sample.

A. Temperature dependence

Figure 1(a) shows the measured phase signals $\delta\varphi$ obtained for the 307-μm-thick sapphire sample for indicated temperatures in the range 295–18 K. The actual travel time decreases with decreasing temperature due to an increased sound velocity.[22] However, since the sample had to be realigned after each temperature step, we could not determine this variation accurately.

At room temperature we find a symmetric, parabolic phase signal, corresponding to a shock wave.[33] Cooling to 200 K, the generation efficiency slightly increases but the wave shape does not significantly change. At 295 and 200 K, the damping $\propto\omega^2$ clearly results in overdamped propagation.

At 100 K, however, the wave shape becomes strongly asymmetric. Velocity differences appear between the front and rear of the wave and are clear indications of nonlinear *and* dispersive propagation.[2] The calculations of Fig. 1(b) demonstrate the formation of (five) acoustic solitons at the front. We note that the solitons are critically damped because of the $\propto\omega$ damping term at 100 K and propagate slower than in the absence of damping. Due to the small arrival time differences, the individual solitons are not resolved.

At 60 K and below, damping has only a minor influence and clear steps appear at the front of the strain wave. Knowing that the phase signal $\delta\varphi_{surface}$ is proportional to the integrated strain passing the surface, steps for $t<0$ at 60 and 18 K point to compressive wave packets separated in space[34] and are characteristic to soliton formation.[12] Calculated soliton arrivals are indicated by numbers in Fig. 1(a) for the 60 K data.

We observe that the final pulse shape depends critically on the magnitude and the frequency dependence of acoustic attenuation. Monitoring nonlinear wave propagation can thus be used to investigate attenuation of high-frequency phonons in weakly attenuating materials.

B. Amplitude measurements at 18 K

Before presenting the phase measurements at 18 K, we consider amplitude (ρ) measurements as a function of pump fluence on the thinnest sample at 18 K. The results are shown in Fig. 2(a). The signals are qualitatively similar to those measured elsewhere.[9,10,12,13]

Since solitons are unipolar and undergo sign change upon reflection at the detection interface, convolution according to Eq. (1) predicts a bipolar amplitude signal with a width equal to the convoluted soliton width. Such bipolar signals indeed show up prior to $t=0$ for fluences >4 mJ/cm^2. At the highest fluence of 8.8 mJ/cm^2, at least four solitons are discernible.

Three typical features of solitons are readily visible. First, their number increases with fluence. This is predicted by Eq. (7), where $\sigma_N \propto s_0^{1/2}$. Second and third, the velocity of soliton i increases with index number i and with pump fluence. This follows from the calculated eigenvalues Eq. (13) and corresponding supersonic soliton velocities v_i in Eq. (10).

Calculated strain waveforms corresponding to curves fitting the measurements are shown in Fig. 2(b). At 8.8 mJ/cm^2, the calculated soliton positions are indicated by arrows. Apparently, for all fluences the slowest one or two solitons are not resolved because they produce only a very small ρ signal. Arrival time variations further decrease the soliton visibility and affect detection of the subsonic high-frequency tail even more dramatically. In Fig. 2(a), for example, the lower two traces show effects of broadening on the calculated signal for a fluence of 8.8 mJ/cm^2.

C. Phase measurements at 18 K

Figures 3(a), 4(a), and 5(a) collect phase measurements for the 123, 307 and 405 μm samples, respectively. In all measurements, clear steps are visible. Their number increases with fluence, in accordance with Eq. (7) and results from the previous section. In contrast to amplitude traces, smaller solitons are resolved in the phase signals. The amplitude of steps in the phase signal, which is a direct measure for the soliton volume V_i, increases with soliton number i. In Fig. 5(c), the steps in the measured trace at 5.9 mJ/cm^2 for the 405 μm sample are shown in more detail. The width of the first step demonstrates that the first soliton fully passes the surface in a time ~1.5 ps. The time of passage increases to ~2.1 and ~2.7 ps for the second and third soliton, respectively, in agreement with Eq. (12). At higher fluences, even sharper steps are expected from Eq. (12) for the first solitons but they apparently wash out.

The increased length of the subsonic dispersive tail with increasing pump fluence confirms that the frequencies in the wave packet have increased for higher pump fluences. Figure

5(d) shows ~500 GHz oscillations at a fluence of 5.9 mJ/cm^2 for the thickest sample, where our temporal resolution at low fluences appeared to be optimal. At higher fluences, where the oscillation frequencies are expected to increase, the oscillation could not be resolved anymore. We can however make an estimate of the frequency content of the tail at the highest fluences. At 405 μm and a fluence of 10.7 mJ/cm^2, the typical length of the tail is ~75 ps, corresponding to a velocity difference Δv of ~23 m/s. From the approximation of the first-order dispersion term,[9] we find that $\Delta v = \beta k^2$. For the typical frequency in the tail $f_{tail} \sim vk/2\pi$ we find 1.5 THz.

V. DISCUSSION

All experimental data presented show excellent agreement with calculations. In this section we discuss calculation details, in particular, the characterization of the generated input pulse width and amplitude at 18 K. In addition, we use inherent properties of solitons for a detailed analysis.

A. Input pulse characterization

Strain pulses launched into the sapphire substrate were calibrated by measuring the generated strain directly on the pump film. The measured width τ was found to be ~3.6 ps for all fluences. This value is typically 0.6 ps shorter than for microcrystalline films, suggesting that the acoustic attenuation is lower and the film quality better. Relative strain amplitude increases in the relevant fluence range as $\propto I_0^{1.7}$, slightly steeper than for a multicrystalline film at room temperature.[18] The superlinear increase can be traced back to the huge rise in temperature in the generation film. For example, at $I_0 = 10$ mJ/cm^2, using a heat capacity C_p of on average 5×10^6 J/(m^3 K),[35] an increase in film temperature of typically $I_0/(C_p \zeta_{pump}) = 1800$ K can be estimated. At these elevated temperatures, an increase in expansion coefficient of Cr by several factors has been observed.[36]

In the numerical calculation, s_0 and τ were left as free fit parameters to allow optimal agreement with the measured data. Values for τ found by the fit routines agree with the measured ~3.6 ps. Fit values for s_0 are collected in Fig. 6(a). Reasonable overlap is obtained between the various sets of measurements. The spread in values for different sets is mainly caused by the $\pm 10\%$ uncertainty in pump fluence. Strain amplitudes and fluence dependences are comparable to those found in earlier experiments.[18]

In absence of damping, a direct estimate for s_0 for a Gaussian derivative [Eq. (8)] can be obtained from the maximum phase signal $\delta\varphi_{\max} = -4\pi\sqrt{e} c v_s s_0 \tau/\lambda$, with c the interferometer contrast. Values for s_0 differed less than 5% from estimates based on the measured $\delta\varphi_{\max}$ for all measurements, except for the 307 μm sample at the highest fluences. Figure 4 shows that for the highest fluences, the first solitons are significantly lower than expected from calculations while the positions are accurately predicted. This suggests spurious scattering at the probe film for this sample.

B. Comparison to measured data

Development of the input pulse shape during propagation was calculated using the known sapphire material parameters and Eq. (5). We subsequently use Eqs. (1)–(3) to determine the measured ρ and $\delta\varphi$ signals.

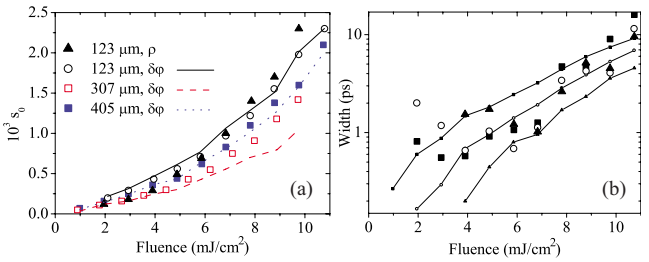

FIG. 6. (Color online) (a) Symbols: fitted strain amplitude s_0 versus pump fluence at 18 K. Fitted temporal width was 3.6 ps in all cases. Lines: values for s_0 derived from maximum phase signal amplitudes. (b) Temporal width determined for the first three soliton signals (squares, circles, and triangles, respectively) and sample thickness 405 μm. Lines are expected nonlinear broadening $\sim 0.07 \delta t_i$ based on measured arrival times t_i.

Experiments show strong additional temporal broadening of the calculated signals. We account for *linear* broadening effects by convoluting the calculated traces with a Gaussian broadening function $(\pi\tau_{br}^2/2)\exp[-2(t-t_0)^2/\tau_{br}^2]$ and $\tau_{br} = (\tau_t^2 + \tau_p^2 + \tau_m^2)^{1/2}$. We include broadening contributions τ_t (probe pulse length) ~180 fs, τ_p (parallelism of the front and rear plane of the sample), specified in Sec. II and τ_m (attenuation in the probe metal film due to electron-phonon interactions[24]) ~100 fs. Thus, τ_{br} is governed by the lack of parallelism. Values of 1.4, 1.0, and 0.6 ps are found for the 123, 307, and 405 μm sample, respectively. At the highest fluences *nonlinear* broadening sets in since 1 ps broadening is by far not enough to account for measured broadening. The characteristic width $w_{meas,i}$ of all detected solitons for the sample thickness of 405 μm was determined and the result is shown in Fig. 6(b). A clear connection between pump fluence and/or soliton index number i and determined width w_{meas} is found.

One cause for nonlinear broadening could be velocity differences due to pump intensity variations. For solitons, the variation in arrival time t_i, δt_i, can be estimated at $\sim 0.07 \times t_i$.[37] For the thickest sample, where $t_1 = -95$ ps and $\delta t_1 \sim 6.5$ ps, exceeding the soliton width ~200 fs by an order of magnitude. The calculated δt_i is plotted in Fig. 6(b) for this sample and shown to be sufficient to explain the measured temporal broadening up to ~10 mJ/cm^2. At the highest fluence of 11 mJ/cm^2, however, additional broadening effects must be invoked. Possibly, higher-order dispersion corrections come into play, affecting the stability of the soliton. We already note that at this fluence, soliton volumes also start to deviate significantly from theory (next section). For even higher fluences, solitons were impossible to detect. Transverse dynamics may come into play, creating sizable arrival time differences over the probe spot.

Our approach works well for the 123 μm ρ and $\delta\varphi$ and 405 μm $\delta\varphi$ data, where temporal broadenings of 0.08 t_i, 0.07 t_i, and 0.07 t_i, respectively, are required to fit experimental traces. For the 307 μm $\delta\varphi$ data a broadening of 0.12 t_i is required, which is again indicative of stronger scattering than for the other samples.

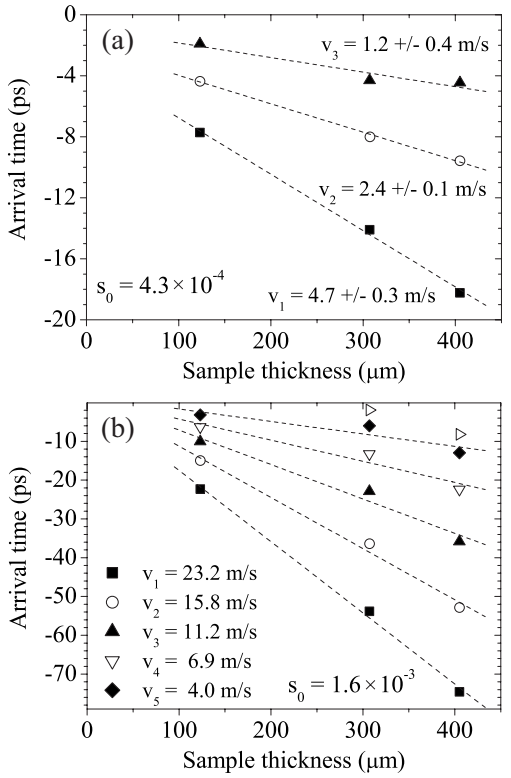

FIG. 7. (a) Position of soliton versus sample thickness for an initial strain wave of amplitude $s_0=4.3\times10^{-4}$ and width $\tau=3.6$ ps. Numbers indicate soliton velocity in meter per second. (b) Like (a) but now for $s_0=1.6\times10^{-3}$. All velocities are determined ±0.1 m/s. No accurate determination of velocity could be performed for the sixth soliton.

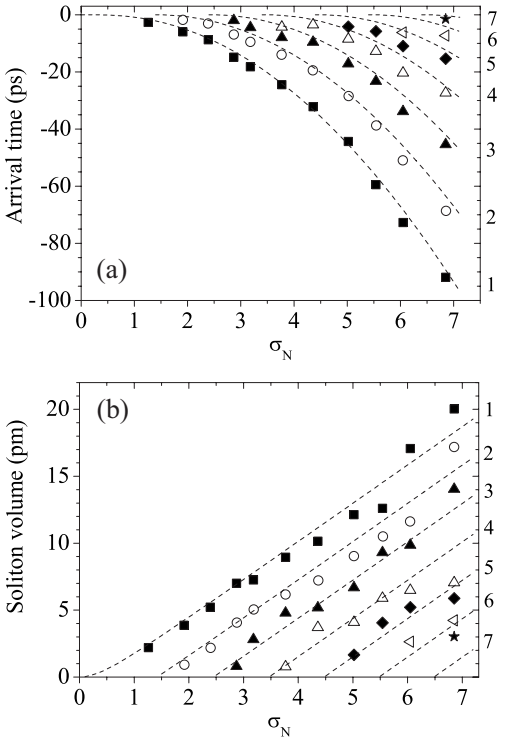

FIG. 8. (a) Position of solitons versus similarity parameter σ_N. Dashed lines give comparison to arrival times predicted by Eqs. (7), (10), and (13). (b) Soliton volume determined from measurements versus similarity parameter σ_N. Dashed lines are soliton volume $V_i=2w_ia_i$ predicted by theory.

Broadening corrections were included in the calculated traces in Figs. 1(a) and 5(a). To demonstrate the importance of the broadening effect, corrected and uncorrected signals are shown both for the amplitude measurement at a fluence of 8.8 mJ/cm^2 in Fig. 2(a) and for the phase at a fluence of 9.8 mJ/cm^2 in Fig. 5(a).

C. Soliton properties

It is interesting to use the measured phase signals at 18 K to analyze the properties of individual solitons. The integrated phase signal step (not taking into account the short and minor contribution $\delta\varphi_{metal}$) of a soliton [Eq. (9)] reads

$$b_i\left\{1+\tanh\left[\frac{(t-t_i)}{w_{meas,i}}\right]\right\}. \tag{14}$$

The soliton velocity v_i in the moving coordinate system can be estimated from the fitted arrival time t_i by t_i/d_{sample}. Here, we take $x_{0,i}$ in Eq. (9) to be zero. For the 405 μm data, where t_i is very large, this certainly is a reasonable approximation. Further, the soliton volume $V_i=2a_iw_i$ can be calculated from b_i by $V_i=(2b_i\lambda)/(8\pi c)$. Finally, the measured signal width $w_{meas,i}$ is the sum of the (typically subpicosecond) soliton width w_i and additional temporal broadening, discussed in the previous section.

First, we analyze the arrival times t_i for the three sample thicknesses at a fixed initial strain amplitude. The result for $s_0=4.3\times10^{-4}$ is shown in Fig. 7(a). Here, $\sigma_N=3.18$ and three solitons form. Arrival times decrease linearly with sample thickness for each soliton. This confirms that solitons move at a constant supersonic velocity. We determine the slope $\Delta t/\Delta d$ and the supersonic velocity $v_i=v_s^2\times\Delta t/\Delta d$, indicated in Fig. 7(a).

For $s_0=1.6\times10^{-3}$, six solitons are detected ($\sigma_N=6.1$). Measured arrival times t_i are presented in Fig. 7(b). Again, a constant supersonic velocity is found. The first soliton at this high fluence has a velocity $v_1=23.2$ m/s. Using Eqs. (11) and (12), we derive an amplitude a_1 for the first soliton of 3.4×10^{-3} [$\sim2s_0$ (Ref. 31)] and a width w_1 of only 200 fs.

Next, we analyze the soliton arrival times t_i and volumes V_i for the sample of 405 μm thickness. Using the s_0 derived earlier, σ_N can be determined for each measurement in Fig. 5. We have plotted the soliton arrival time t_i and volume V_i versus σ_N in Figs. 8(a) and 8(b), along with the expected dependence from the theory in Sec. III. Excellent agreement is found. For $\sigma_N\gg i$, v_i is found from Eqs. (10) and (13) to depend quadratically on σ_N. On the other hand, $V_i\propto v_i^{1/2}$ and thus depends linearly on σ_N. Both dependencies are accurately reproduced in Fig. 8.

VI. CONCLUSIONS

In conclusion, we have succeeded in observing soliton formation in sapphire slabs of different thicknesses in inter-

ferometric pump-probe experiments. A high degree of parallellism of the sample front and rear planes, and the quality of the Cr detection films appear to be crucial for successful soliton detection. At 100 K, critical damping occurs preventing full soliton formation. However, at 60 K, solitons fully develop and propagate virtually undamped. Extrapolation of the damping determined at these temperatures suggests soliton formation and propagation at liquid nitrogen temperatures in sapphire. This observation may prove to be relevant for the practical use of acoustic solitons in nanoultrasonic material characterization.

Up to seven solitons in the train are distinguished at the highest fluence of 11 $\mathrm{mJ/cm^2}$, for a strain pulse with input amplitude 2.1×10^{-3} and temporal width 3.6 ps. At moderate pump fluences, we have directly measured the temporal width of single solitons of only 500 fs in sapphire, corresponding to a spatial extent as small as 5 nm. From accurately measured supersonic soliton velocities, a minimal soliton width of 200 fs (corresponding to <2 nm width) can be inferred at the highest fluences. Such time and length scales open the way to acoustic manipulation of nanometer-sized structures on a subpicosecond time scale.[38]

Frequencies of 500 GHz are observed in the high-frequency tail while frequencies up to 1.5 THz can be inferred. Direct observation of frequencies >500 GHz in both compressive and tensile parts is washed out by nonlinear broadening effects related to power fluctuations of the laser. The recently demonstrated high-bandwidth piezoelectric strain gauge may well prove a challenging new tool to disclose the full frequency acoustic spectrum present in soliton trains.[39]

All measured traces agree excellently with numerical calculations based on the Korteweg-de Vries equation. Furthermore, measured properties of the generated solitons match in detail with the exact relations between soliton amplitude, width, and velocity of the Korteweg-de Vries solutions.

ACKNOWLEDGMENTS

We thank Matt Highland and David Cahill for growing high-quality chromium films on the used samples. C.R. de Kok and P. Jurrius are acknowledged for their technical assistance. This work is part of the research program of the "Stichting voor Fundamenteel Onderzoek der Materie (FOM)," which is financially supported by the "Nederlandse Organisatie voor Wetenschappelijk Onderzoek (NWO)."

*j.i.dijkhuis@uu.nl

[1] C. Kittel, *Introduction to Solid State Physics*, 7th ed. (Wiley, New York, 1996).
[2] H.-Y. Hao and H. J. Maris, Phys. Rev. Lett. **84**, 5556 (2000).
[3] F. D. Murnaghan, *Finite Deformations of an Elastic Solid* (Wiley, New York, 1951).
[4] A. R. Osborne and T. L. Burch, Science **208**, 451 (1980).
[5] L. F. Mollenauer, R. H. Stolen, and J. P. Gordon, Phys. Rev. Lett. **45**, 1095 (1980).
[6] G. O. Ludwig, J. L. Ferreira, and Y. Nakamura, Phys. Rev. Lett. **52**, 275 (1984).
[7] K. E. Strecker, G. B. Partridge, A. G. Truscott, and R. G. Hulet, Nature (London) **417**, 150 (2002).
[8] D. J. Korteweg and G. de Vries, Philos. Mag. **39**, 422 (1895).
[9] H.-Y. Hao and H. J. Maris, Phys. Rev. B **64**, 064302 (2001).
[10] W. Singhsomroje and H. J. Maris, Phys. Rev. B **69**, 174303 (2004).
[11] B. C. Daly, T. B. Norris, J. Chen, and J. B. Khurgin, Phys. Rev. B **70**, 214307 (2004).
[12] E. Péronne and B. Perrin, Ultrasonics **44**, e1203 (2006).
[13] P. Hess and A. M. Lomosonov, Ultrasonics **50**, 167 (2010).
[14] O. L. Muskens and J. I. Dijkhuis, Phys. Rev. Lett. **89**, 285504 (2002).
[15] O. L. Muskens, A. V. Akimov, and J. I. Dijkhuis, Phys. Rev. Lett. **92**, 035503 (2004).
[16] O. L. Muskens and J. I. Dijkhuis, in *Non-Equilibrium Dynamics of Semiconductors and Nanostructures*, edited by K.-T. Tsen (CRC Press, Boca Raton, 2005), p. 15.
[17] B. B. Kadomtsev and V. I. Petviashvili, Sov. Phys. Dokl. **15**, 539 (1970).
[18] P. J. S. van Capel and J. I. Dijkhuis, Appl. Phys. Lett. **88**, 151910 (2006).
[19] T. Saito, O. Matsuda, and O. B. Wright, Phys. Rev. B **67**, 205421 (2003).
[20] T. Tachizaki, T. Muroya, O. Matsuda, Y. Sugawara, D. H. Hurley, and O. B. Wright, Rev. Sci. Instrum. **77**, 043713 (2006).
[21] T. Saito, O. Matsuda, and O. B. Wright, Phys. Rev. B **69**, 239902(E) (2004).
[22] H.-Y. Hao and H. J. Maris, Phys. Rev. B **63**, 224301 (2001).
[23] F. Watanabe, D. G. Cahill, B. Gundrum, and R. S. Averback, J. Appl. Phys. **100**, 083519 (2006).
[24] J. W. Tucker and V. W. Rampton, *Microwave Ultrasonics in Solid State Physics*, 1st ed. (North-Holland, Amsterdam, 1972).
[25] B. A. Auld, *Acoustic Fields and Waves in Solids*, 2nd ed. (Robert E. Krieger, Malabar, 1990), Vol. 1.
[26] M. Pomerantz, Phys. Rev. **139**, A501 (1965).
[27] I. S. Ciccarello and K. Dransfeld, Phys. Rev. **134**, A1517 (1964).
[28] C. Herring, Phys. Rev. **95**, 954 (1954).
[29] E. P. N. Damen, A. F. M. Arts, and H. W. de Wijn, Phys. Rev. B **59**, 349 (1999).
[30] W. Chen and S. Holm, J. Acoust. Soc. Am. **115**, 1424 (2004).
[31] O. L. Muskens and J. I. Dijkhuis, Phys. Rev. B **70**, 104301 (2004).
[32] V. I. Karpman, *Non-linear Waves in Dispersive Media*, 1st ed. (Pergamon Press, Oxford, 1975).
[33] P. J. S. van Capel, H. P. Porte, G. van der Star, and J. I. Dijkhuis, J. Phys.: Conf. Ser. **92**, 012092 (2007).
[34] O. Matsuda, T. Tachizaki, T. Fukui, J. J. Baumberg, and O. B. Wright, Phys. Rev. B **71**, 115330 (2005).
[35] J.-O. Andersson, Int. J. Thermophys. **6**, 411 (1985).
[36] N. A. Dubrovinskaia, L. S. Dubrovinsky, S. K. Saxena, and B. Sundman, CALPHAD: Comput. Coupling Phase Diagrams Thermochem. **21**, 497 (1997).

[37] We assume that for soliton i, $\delta t_i/t_i = \delta v_i/v_i = \delta a_i/a_i \sim \delta s_0/s_0$. When the variations in pump fluence are $\delta I_0 \sim \pm 2\%$ and taking into account that $s_0 \sim I_0^{1.7}$, we derive for soliton i that $\delta v_i \sim 2 \times 0.02 \times 1.7 \times v_i$.

[38] A. V. Akimov, A. V. Scherbakov, D. R. Yakovlev, C. T. Foxon, and M. Bayer, Phys. Rev. Lett. **97**, 037401 (2006).

[39] M. R. Armstrong, E. J. Reed, K.-Y. Kim, J. H. Glownia, W. M. Howard, E. L. Pines, and J. C. Roberts, Nat. Phys. **5**, 285 (2009).